Chemical Science

ROYAL SOCIETY OF CHEMISTRY

EDGE ARTICLE

View Article Online
View Journal | View Issue

Cite this: *Chem. Sci.*, 2026, **17**, 7599

All publication charges for this article have been paid for by the Royal Society of Chemistry

Compatible bridged interphase with enhanced Li ion migration for durable quasi-solid-state lithium metal batteries

Peng Chen,[a] Hui Wang,[a] Tianyu Wei,[a] Shengliang Zhang,[a] Bing Ding,[abc] Hui Dou *[abc] and Xiaogang Zhang *[abc]

Solid-state lithium metal batteries suffer from incompatible interfacial electrochemistry introduced by mismatched lithium ion diffusion rates across the anode/electrolyte, which leads to interface degradation and dendrite formation. Here, we propose an interfacial ion migration modulator to bridge the Li ion transport pathway between ceramic–polymer composite electrolytes and Li metal using a series of different lithiophilic nanoscale metals. With the aid of comprehensive theoretical simulations, different metals are screened *via* spectroscopic measurements as well as electrochemical tests, where Pt acts best and *in situ* forms a Li–Pt alloy solid-electrolyte interphase layer with a coherent crystal structure during the electrochemical reaction, reducing the internal Li diffusion energy barrier. As investigated, the distribution of relaxation time analyses reveals that the Li–Pt alloy-based interfacial ion migration modulator regulates and balances the interfacial ion transport and nucleation rate, inhibiting defect formation. Consequently, the symmetric cell with the Pt modulator lasts for 1900 h with a low overpotential of 10.7 mV. Moreover, the Pt@polymer electrolyte-based quasi-solid-state lithium metal battery assembled with the $LiFePO_4$ cathode displays greatly improved cycling stability (154.6 mAh g^{-1} at the 150th cycle, 0.2C). This work clarifies the role of the essential interfacial ion migration modulator in paving the way towards extending the interface lifespan of SSLMBs.

Received 19th January 2026
Accepted 15th February 2026

DOI: 10.1039/d6sc00515b

rsc.li/chemical-science

1 Introduction

Polymer electrolyte-based quasi-solid-state lithium metal batteries (QSSLMBs), which combine high-capacity Li metal anodes with robust polymer-based solid electrolytes, have been considered as a satisfactory choice to simultaneously offer both high energy density and superior safety.[1–3] However, the initial non-conformal "point-to-point" interface contact and the voids formed due to Li stripping lead to high overpotential and interfacial instability, which in turn trigger detrimental interfacial side reactions and uncontrolled Li dendrite growth (Fig. 1a).[4,5] Constructing stable interfacial ion transport channels and regulating the interfacial ion diffusion processes are crucial for achieving high-performance QSSLMBs.[6,7]

As is known, the interphase engineering between the Li anode and polymer-based solid electrolytes, typically composed of components such as LiF and Li_2O, plays a crucial role in interfacial processes. The constituent species, which exhibit different affinities for Li metal, directly govern the thermodynamic surface and modulate the energy barriers for interfacial Li^+ diffusion and nucleation.[8,9] For example, Li *et al.* revealed that interfacial ionic transport across the solid-electrolyte interphase (SEI) layer is around 10^{-6} cm^{-2} s^{-1} to $\sim10^{-9}$ cm^{-2} s^{-1}, causing a sharp rise in interfacial impedance (Fig. S1).[8] Thus, enhancing the interfacial ionic transport kinetics contributes to balancing the interface electrochemistry to achieve uniform interfacial Li^+ deposition. However, interface deterioration still occurs even when the interfacial ionic transport rate of the SEI has been greatly enhanced through film-forming agents or self-sacrifice methods.[10,11] Moreover, defects in the SEI will form and accumulate during Li stripping/plating due to inadequate replenishment of Li loss, intensifying interface degradation and Li metal fatigue.[12] Therefore, it is of significance to simultaneously enhance the interfacial ionic transport rate and suppress the formation of interface defects.

Herein, we propose an interfacial ion migration modulator to bridge the Li ion transport pathway between ceramic–polymer composite electrolytes (CPCEs) and Li metal using a series of different lithiophilic nanoscale metals. As a proof-of-concept, different metal modification layers of Cu, Ni, Ag, Au, and Pt were compared on the metallic Li surface respectively, and it is

[a]*Jiangsu Key Laboratory of Electrochemical Energy Storage Technologies, College of Materials Science and Technology, Nanjing University of Aeronautics and Astronautics, Nanjing 210016, P. R. China. E-mail: dh_msc@nuaa.edu.cn; azhangxg@nuaa.edu.cn*

[b]*National Key Laboratory of Mechanics and Control for Aerospace Structures, Institute for Frontier Science, Nanjing University of Aeronautics and Astronautics, Nanjing 210016, P.R. China*

[c]*Shenzhen Research Institute, Nanjing University of Aeronautics and Astronautics, Shenzhen 518000, China*

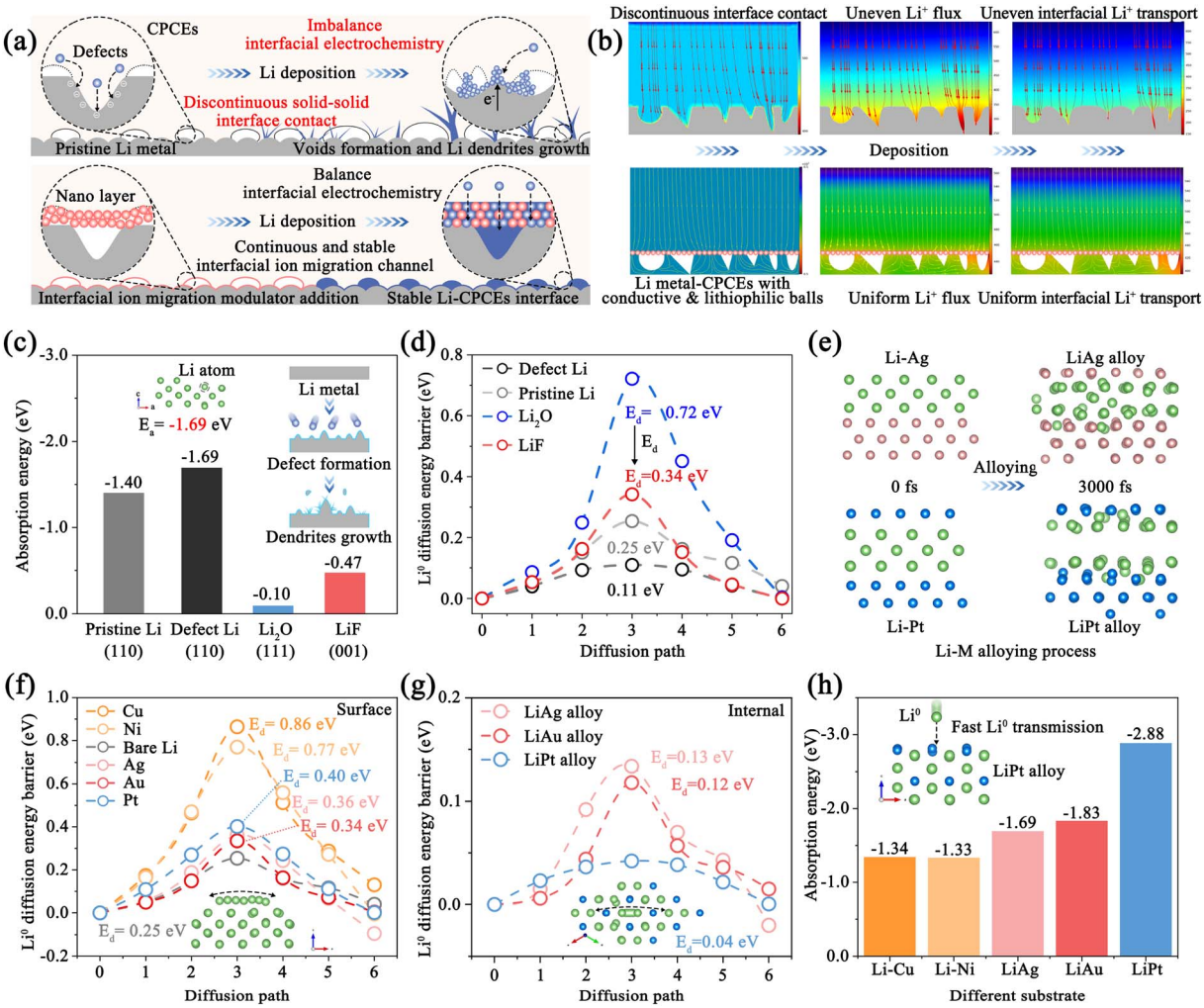

Fig. 1 Theoretical basis of the interfacial ion migration modulator. (a) Schematic diagram illustrating the CPCE-based QSSLMBs without/with the interfacial ion migration modulator. (b) COMSOL simulation of Li^+ flux at the interface between the CPCEs and Li anode without/with the interfacial ion migration modulator. (c) Adsorption energy and (d) diffusion energy barriers for Li^0 on the surface of pristine Li (110), defect Li (110), Li_2O (111) and LiF (001) substrates. (e) AIMD simulation. Diffusion energy barriers for Li^0 on the (f) surface and (g) internal of different metal substrates. (h) Adsorption energy barriers for Li^0 on the surface of different interfacial ion migration modulators.

found that a stable physically/chemically interfacial ion migration modulator is constructed, achieving continuous and rapid interfacial Li^+ transport and Li nucleation (Fig. 1a). During the Li stripping and plating process, stable interfacial Li–M alloy layers are *in situ* formed on the CPCEs, acting as an ion migration modulator to enhance the interfacial contact and inhibit defect formation (Fig. S2). More importantly, calculation and experimental results show that this interfacial ion migration modulator accelerates Li^+ diffusion and balances the interfacial electrochemistry, promoting uniform Li deposition and achieving satisfactory cycling stability. In particular, the Li|Pt@CPCEs|$LiFePO_4$ (LFP, 1C = 170 mAh g^{-1}) based cell achieves a high specific capacity of 154.6 mAh g^{-1} at the 150th cycle (0.2C, 30 °C). Our result offers an understanding of the working mechanism of the interfacial ion migration modulator between CPCEs and Li anode, which are important for designing high-performance QSSLMBs with long cycle stability.

2 Results and discussion

2.1 Theoretical basis of defect and ionic transport rate effects on CPCEs–Li anode interface electrochemistry

Model CPCEs with ceramic (LLZTO) and polymer (PVDF-HFP) were used in this work, and were investigated in detail in our previous reports.[5,13] As shown in Fig. S3a and b, the microscopic surface structure of pristine Li metal and CPCEs prepared by the solution casting method is rough, which leads to discontinuous solid–solid interface contact in the QSSLMBs.[14,15] Initially, COMSOL was carried out to analyze the effect of the structure–activity relationship of interfacial contact on Li^+ transport. As illustrated in Fig. 1b, the discontinuous interfacial contact in QSSLMBs evokes the disordered interfacial electric field, triggering uneven Li^+ flux and interfacial Li^+ transport, during the Li deposition process.[4] Meanwhile, Li^+ tends to accumulate and preferentially deposit in the defect sites rather than on the smooth surface, which indicates that defects and voids might

act as nucleation sites for dendrite growth.[6] However, the interface modification and the plating behaviors are much smoother. Then, the CPCE-based Li||Li symmetric cell was assembled to investigate the interfacial Li stripping/plating behaviors. When the stripping capacity reaches 0.1 mAh cm^{-2} at a current density of 0.05 mA cm^{-2}, *in situ* electrochemical impedance spectroscopy (EIS) and distribution of relaxation time (DRT) results suggest that the polarization potential increase originates from the rising interfacial impedances, which verifies the continuous interface deterioration resulting from the presence of interfacial electrochemical imbalance (Fig. S4).[16,17] Satisfactory interface stability can be realized by reducing the interfacial impedance. Thus, conductive and lithiophilic metal nanoparticle models were introduced at the interface between the rough Li anode and CPCEs. As shown in Fig. 1b, interfacial Li^+ flux is dynamically adjusted by bridging the interfacial Li^+ transport pathway during the Li deposition process.

Since Li^+ transport through the SEI and CPCEs accounts for the majority of the interfacial impedance, the dramatic increase in polarization potential shows that the SEI and CPCEs impede Li^+ transport during stripping/plating.[18] To gain deeper insight, we constructed computational models to simulate Li migration on various SEI components (*e.g.*, LiF, Li_2O) and Li surfaces (with and without defects) and quantitatively evaluate the associated adsorption and migration energy barriers (Fig. S5 and S6).[9,19] Fig. 1c shows that Li adsorption is most favorable on defect Li with the lowest energy (−1.69 eV) aided by Li vacancies, which is lower than that of pristine Li (−1.40 eV), LiF (−0.47 eV) and Li_2O (−0.10 eV). Moreover, the optimal migration pathways for Li diffusion on the surface of defect Li exhibit a lower energy barrier (0.11 eV) than pristine Li (0.25 eV), Li_2O (0.72 eV), and LiF (0.34 eV), whereas Li^+ migration within the SEI is lower, especially in Li_2O (0.20 eV) and LiF (0.66 eV) (Fig. S7). This disparity causes Li^+ to be reduced at defect sites with rich electrons and subsequently deposit as Li^0 at the defective Li–Li_2O/LiF interface, thereby inducing dendrite growth and SEI rupture. Thus, the defects accumulate on the Li surface and voids form at the CPCE side due to the unbalanced interfacial electrochemistry, leading to continuous interfacial resistance and polarization potential increase.[20,21]

2.2 Theoretical basis of the interfacial ion migration modulator

A well-engineered interface ion transport channel is critical in QSSLMBs, as it governs the interfacial electrochemistry and directs Li deposition/stripping behavior.[22,23] An ideal interface ion transport channel, characterized by high lithiophilicity, low energy barriers for internal and surface Li^0 diffusion, and high mechanical strength, promotes uniform Li^+ deposition and lateral Li^0 diffusion, thereby guiding stable cycling performance.[12,24] To verify this, a series of 5 metal materials: Cu, Ni, Ag, Au and Pt as CPCE modification layers were studied, which can form an artificial Li–M nonalloy/alloy SEI layer to construct the interface ion migration modulator. This list is representative because some of the conductive metals are Li non-alloyable (Cu, Ni) and others are alloyable with Li. To understand the interfacial electrochemical regulation mechanism, theoretical calculation was essential for investigating the interfacial Li^+ transport and Li^0 nucleation behavior.

Considering that there are two states of ion migration modulator in the electrochemical process, we established different models for Li adsorption and migration in both metal phases and alloy phases to fully explain the fundamental mechanism, respectively. *Ab initio* molecular dynamics (AIMD) simulations in Fig. 1e, S8 and S9 reveal that the alloying processes of Li–Ag and Li–Au are faster after 1500 fs compared with Li–Pt (3000 fs).[25] The interfacial energy decreases with the increasing degree of alloying between the Li–M alloy layer and Li anode, indicating that the migration energy barriers of Li^+ can be reduced. The migration energy barriers on the various metal substrate were calculated (Fig. S10).[26–28] The energy barriers for Li migration on Ag, Au, Pt substrates (0.34, 0.36 and 0.40 eV) are markedly lower than that on Cu and Ni substrates (0.86 and 0.77 eV), yet all are higher than that on pristine Li metal (Fig. 1f). The elevated barriers relative to Li metal, imparted by the Li-metal interfacial heterogeneities, indicate that a high nucleation barrier is obtained during the initial Li deposition. The formation of the Li–M alloy endows the substrate with high lithiophilicity to reduce the nucleation energy barrier, while its coherent crystal structure creates efficient ion transport pathways.[29,30] For instance, the Li–Pt alloy can reduce the internal Li diffusion energy barrier (0.04 eV *vs.* 0.45 eV), realizing the rapid transport of Li inside the SEI (Fig. 1g and S11–S13). However, pristine Li has a lower diffusion energy barrier of 0.25 eV for Li^0, indicating that Li tends to deposit on the Li metal surface rather than at the interface between the SEI and CPCEs. Meanwhile, the adsorption energies of Li on the Li–Ag, Li–Au, and Li–Pt alloy substrates (−1.69, −1.83 and −2.88 eV) are higher than those of Li–Cu, Li–Ni nonalloy layers (−1.34 and −1.33 eV) and pristine Li (−1.40 eV) due to the good interfacial compatibility and thermodynamic match (Fig. 1h and S14).[31]

2.3 Formation of the interfacial ion migration modulator

Theoretically, a stable and rapid ionic transport channel can avoid the interfacial failure of QSSLMBs. Thus, the interfacial ion migration modulator was prepared by vacuum deposition with corresponding thin coating onto the CPCE substrate (named M@CPCEs), exploring the interfacial electrochemistry under practical working conditions (Fig. 2a). By controlling the electrical current and sputtering time, the metal modification layer with a thickness of ~52.7 nm was prepared as the interfacial ion migration modulator to improve the interfacial electrochemistry. Compared with bare CPCEs, M@CPCEs shows a distinct metallic luster in Fig. S15 and S16. X-ray photoelectron spectroscopy (XPS) was used to verify the existence of the metal modification layer on CPCEs, as shown in Fig. 2c and S17.

The pristine CPCE surface exhibits inherent roughness and porosity, attributable to the LLZTO fillers and voids (Fig. S18). This morphology reduces the interfacial ion transport channels and creates an imbalance in the interfacial electrochemical

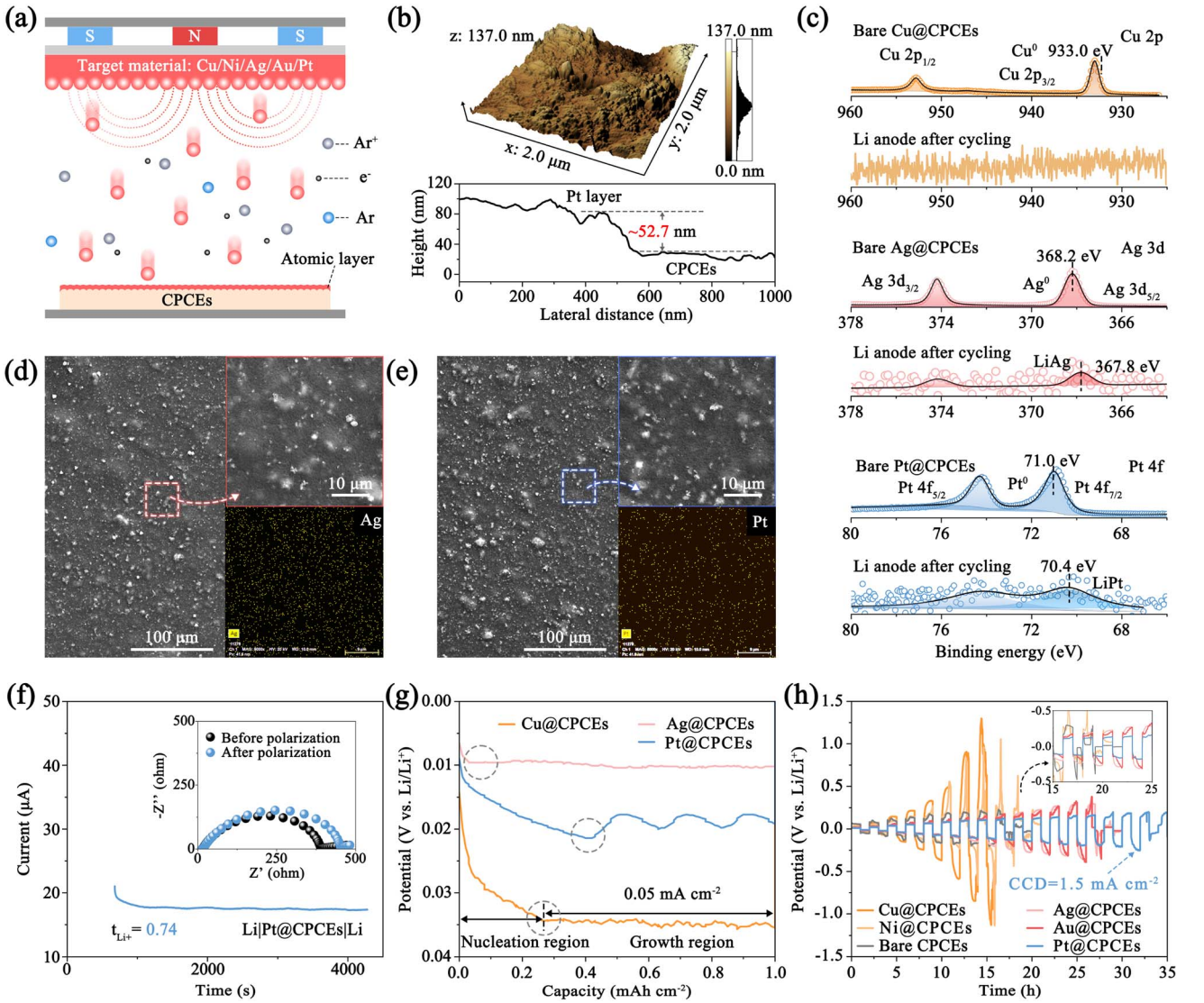

Fig. 2 Characterization of the interfacial ion migration modulator. (a) Schematic diagram of the vacuum deposition of metal on CPCEs. (b) Atomic Force Microscope (AFM) image of Pt@CPCEs. (c) XPS profiles of Cu 2p, Ag 3d and Pt 4f of M@CPCEs, and XPS profiles of Cu 2p, Ag 3d and Pt 4f of the interfacial ion migration modulator on the Li anode after stripping/plating for 50 h (etching for 100 s). SEM images and corresponding elemental mapping of (d) Ag@CPCEs and (e) Pt@CPCEs. (f) Chronoamperometry curve and AC impedance spectra before and after polarization of the Li|Pt@CPCEs|Li symmetric cell. (g) Voltage profiles of Li|M@CPCEs|Li symmetric cells during Li deposition at a current density of 0.05 mA cm^{-2}. (h) Voltage evolutions of Li|M@CPCEs|Li symmetric cells at step-increasing currents.

reaction, ultimately leading to performance degradation (Fig. S18c),[6] while, as shown in Fig. 2d, e and S19–S23, the introduced metal modification layer conformally coats this rough surface without altering its underlying microstructure. Elemental mappings further confirm the uniform distribution of metal layers across the CPCEs. This uniform sputtering of nano-metal particles on the surface of CPCEs enlarges the interfacial contact area, enabling continuous interfacial ion transport. Moreover, the lithiophilic metal nanoparticles (*e.g.*, Ag, Au, Pt) *in situ* form the Li–M alloy phase to construct the interfacial ion migration modulator with a low migration energy barrier during the electrochemical process, which can balance the interfacial electrochemical rate and inhibit the interfacial deterioration (Fig. 2f).[32]

2.4 Spatial control of interfacial Li diffusion and deposition

To further reveal the role of the interfacial ion migration modulator in regulating the interfacial Li^+ diffusion and nucleation, the M@CPCE-based Li||Li symmetric cells were assembled to investigate the electrochemical performance (Fig. S24). Fig. 2g and S25 show that Pt@CPCEs exhibits higher Li^+ transference number (t_{Li^+} = 0.74) than Cu@CPCEs (0.41), CPCEs (0.49), and Ag@CPCEs (0.61) due to the high adsorption energy of Li^0 on the Li–Pt alloy substrate and the anion anchoring effect of LLZTO.[5] The rapid Li^+ transference of M@CPCEs can accelerate the interfacial ion transport, realizing uniform interfacial Li deposition. Li atom was galvanostatically deposited on the M@CPCE protected Li anode at a current

density of 0.05 mA cm^{-2} to validate the interfacial Li nucleation behavior.[7,30] Fig. 2h shows that a significant potential dip is formed at the beginning of Li atom deposition, followed by a standing nucleation platform. Among the M@CPCE-based Li||Li symmetrical cells, metals such as Ag and Au can rapidly form Li–M alloy compounds. This process reduces the thermodynamic mismatch between Li and the resulting Li–M alloy, leading to a low nucleation barrier, compared to the Cu@CPCE-based symmetric cell, which shows a high polarization potential at the critical current density despite its high nucleation kinetics. The modification layers of different metals act as an interfacial ion migration modulator during cycling, effectively reducing nucleation barriers and facilitating rapid Li nucleation and diffusion. Thus, the Pt@CPCE-based symmetric cell achieves the lowest polarization potentials and sustains an excellent high current density of 1.5 mA cm^{-2} for Li stripping/deposition due to the lowest internal/surface Li migration energy barriers.

To verify the superiority of the interfacial ion migration modulator, M@CPCE-based Li||Li symmetric cells were subjected to long-term galvanostatic cycling at 0.1 mA cm^{-2}. In the case of the Li|Pt@CPCEs|Li symmetric cell (Fig. 3a), an initial rise in polarization to 19.2 mV at 180 h is observed due to the Li–Pt alloying process. The formation of continuous and stable Li–Pt alloy interfacial layers significantly enhances the ion transport kinetics, enabling the cell to cycle for 1900 h without short-circuiting (10.7 mV). Conversely, Cu@CPCE and CPCE-based cells both suffer from interfacial deterioration with higher initial polarization potentials due to inferior ion transport kinetics and imbalance in interfacial electrochemistry. Furthermore, the disordered Li deposition introduces dendrite growth, leading to short circuits before 900 h. This is more obvious at 0.5 mA cm^{-2}. The Pt@CPCE-based cell maintains stable plating/stripping over 600 h with a low polarization potential of 135.3 mV (Fig. 3b). By contrast, the Cu@CPCE-based Li||Li symmetric cells experience a short circuit after only 320 h.

To uncover the working mechanism of the interfacial ion migration modulator, further investigation was conducted on Li||Li symmetric cells. The galvanostatic charge–discharge voltage profiles in Fig. 3c and S26 verify that discontinuous physical contact between the CPCEs and Li anode induces undesirable side reactions, leading to a gradual increase in interfacial polarization potential.[15] The introduction of the interfacial ion migration modulator (Ag, Au, Pt, *etc.*) with high lithiophilicity establishes stable and continuous interfacial ion migration pathways, thereby enabling interfacial electrochemical balance. Crucially, the alloying process with these metals reduces both Li^+ diffusion and nucleation barriers, resulting in a steady decrease in polarization potential, especially in the Pt@CPCE-based cell. Conversely, modification layers such as Cu and Ni, which possess excessively high nucleation barriers and low ion transport rates, promote uneven Li nucleation and exacerbate interfacial side reactions. To further investigate the Li deposition/stripping kinetics with the function of the interfacial ion migration modulator, analysis of the M@CPCE-based symmetric cell after cycling was performed. The digital pictures and SEM images in Fig. 3d and S27a clearly show that the unmodified Li|CPCEs|Li developed a matte Li surface covered with substantial Li dendrites. By contrast, the Li surface protected by Ag@CPCEs and Pt@CPCEs remains relatively smooth. This morphological superiority is directly linked to the lower interfacial atomic diffusion and nucleation barriers (Fig. S27a–c). What's more, on the Li metal surface protected by the Pt and Ag modification layer, Li still nucleates and grows as fine nuclei at the surface defects. This observation confirms that the interfacial ion migration modulator enhances the nucleation kinetics of Li. Moreover, XRD analyses of the cycled Li metal anode in Li|M@CPCEs|Li cells indicate that Ag@CPCEs and Pt@CPCEs can promote rapid lateral Li^+ diffusion on the Li metal surface, promoting preferential nucleation and growth along the (110) crystal plane (Fig. 3e).[33] By contrast, the unbalanced interfacial electrochemistry on CPCEs leads to sluggish Li deposition kinetics, causing Li to deposit and grow longitudinally along the (200) crystal plane, gradually deteriorating the interface.

The corresponding elemental mappings and XPS analysis of the cycled Li metal from the unmodified cell confirm that the unbalanced interfacial electrochemistry induces continuous interfacial side reactions, resulting in substantial accumulation of Li_2CO_3, dendrites and defects (Fig. S28 and S29). The cycled Li metal with Pt@CPCEs exhibits a stronger F signal, corresponding to the formation of LiF due to the deposition regulated by Pt@CPCEs (Fig. S30 and S31). To further verify the working mechanism of the interfacial ion migration modulator, XPS depth etching and Time of Flight Secondary Ion Mass Spectrometry (TOF-SIMS) were conducted to analyze the cycled Li metal.[34] As shown in Fig. 3f, an *in situ* formed SEI layer, with LiF, Li_2CO_3, and Li_2O, is distributed on the surface of the Li metal protected by Pt@CPCEs, which can suppress electron tunneling (Fig. S32 and S33).[35] As expected, the amount of Li_2CO_3 gradually decreases, while the amounts of LiF and Li_2O gradually increase, with increase in the etching depth. More importantly, certain characteristic peaks of the Li–Pt alloy and Li^0 gradually appear in the deeper region, indicating the formation of a Li/Li–Pt alloy/Li_2O–LiF sandwich structure. This configuration was further verified by TOF-SIMS analysis (Fig. 3h, S34 and S35). The optimized interface ion transport and deposition kinetics enabled by the interfacial ion migration modulator facilitate the uniform formation of a protective SEI layer rich in LiF and Li_2O between the Li–Pt alloy layer and CPCEs, enabling stable multi-gradient ionic transport and achieving uniform Li deposition. EDS analysis reveals significantly higher Pt content in etched areas compared to unetched regions, confirming the formation of the Li–Pt alloy with a dense SEI layer on the Li–Pt alloy/Li anode. Moreover, the synergistic effect of the LiF/Li_2O-rich SEI and Li–Pt alloy regulates the interfacial Li deposition/stripping kinetics while balancing electrochemical processes, promoting uniform Li nucleation (Fig. 3i and S35).[31] Conversely, the lithiophobic and non-alloying Cu accelerates interface degradation. Increasing formation of Li_2CO_3 and dead Li ultimately causes irregular etching in the Li anode (Fig. S36). Therefore, the introduction of the artificial lithiophilicity metal interface layer can construct

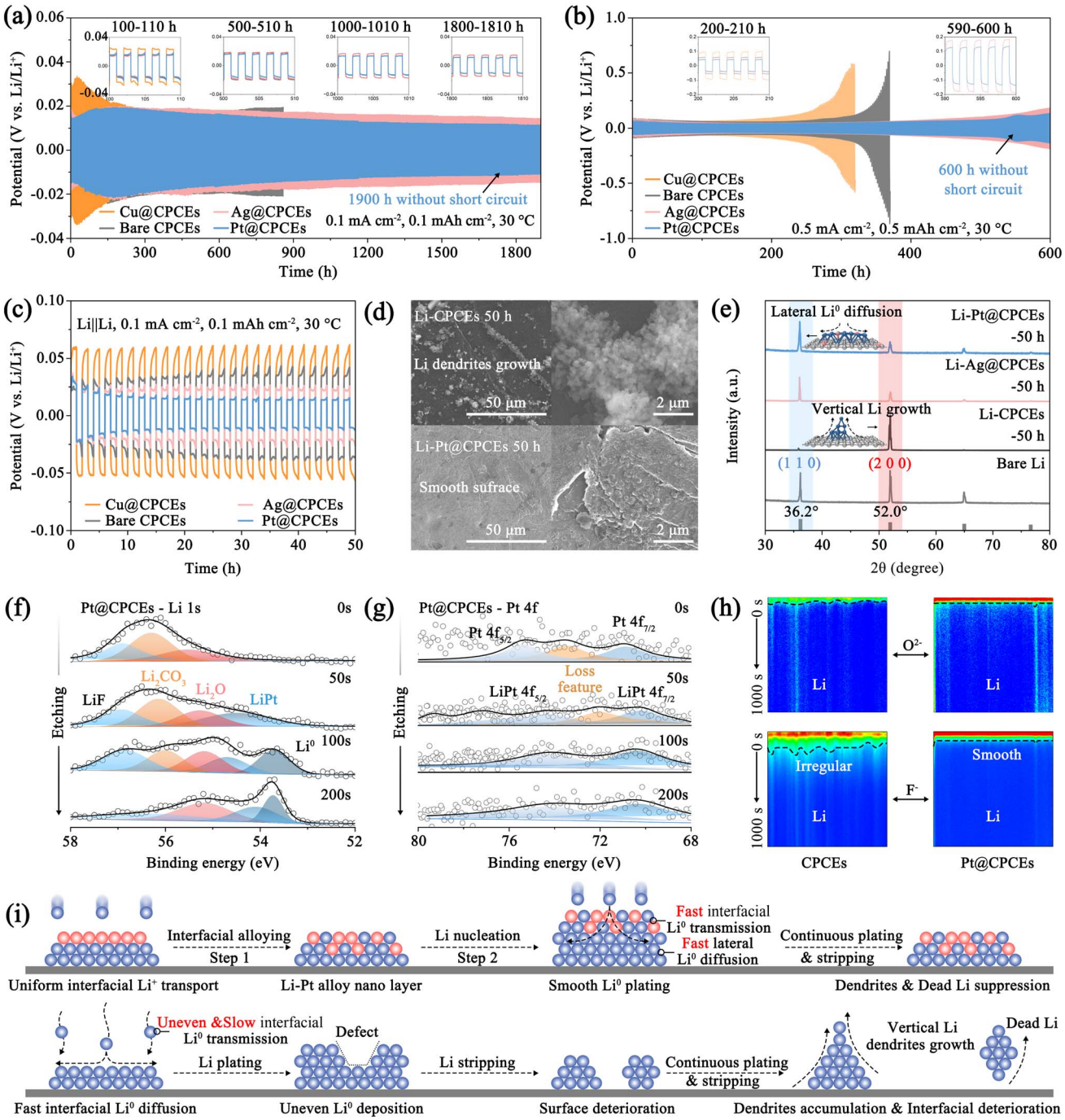

Fig. 3 Analysis of the working mechanism of the interfacial ion migration modulator. Voltage profiles of Li|M@CPCEs|Li symmetric cells under a cyclic current of (a and c) 0.1 mA cm^{-2}, 0.1 mAh cm^{-2} and (b) 0.5 mA cm^{-2}, 0.5 mAh cm^{-2}, at 30 °C. (d) SEM images of the Li metal interface within Li||Li symmetric cells after cycling. (e) XRD of bare Li metal and Li metal within Li|M@CPCEs|Li symmetric cells after cycling. XPS profiles of (f) Li 1s and (g) Pt 4f on the cycled Li metal with etching. (h) The TOF-SIMS sputtered volumes of Li metal without/with Pt@CPCEs. (i) Schematic diagram of the working mechanism of the interfacial ion migration modulator.

continuous ionic transport channels and regulate interfacial electrochemical behavior, thereby achieving satisfactory electrochemical performance. On the basis of the theoretical calculation simulation and experimental results, the working mechanism of interfacial ion migration modulator based QSSLMBs is inferred as follows. During Li deposition, Li^+ tends to deposit as Li^0 inside the interfacial ion migration modulator after obtaining electrons due to the low internal diffusion energy barrier, rapidly diffusing to the anode–interfacial ion migration modulator interface. A competitive adsorption pathway for Li^0 is established between Li metal and the Li–M alloy, facilitating its fast and uniform diffuse. This fast interfacial diffusion, supported by robust interfacial connectivity, in turn inhibits the nucleation and growth of defects and voids,

ultimately preventing mechanical fatigue and associated interface failure.[12]

To investigate the dynamic processes, electrochemical impedance spectroscopy (EIS) and distribution of relaxation time (DRT) analyses were performed on Li|M@CPCEs|Li symmetric cells at 0.05 mA cm^{-2}. As shown in Fig. 4a–c, S37 and S38, the Cu@CPCE-based Li||Li symmetric cells exhibit significantly higher polarization potentials (~35 mV) than Ag@CPCEs (~20 mV) and Pt@CPCEs (~19 mV) after plating/stripping for 4 h. More importantly, the Li–Pt alloy layer enhances Li$^+$ transport kinetics across the CPCEs/SEI/Li interface, enabling stable and continuous ion transmission. The transmission and deposition behaviors of Li in the two capacitor-type interface layers were elucidated through DRT analysis (Fig. 4d).[16,36] The resistance can be categorized into: (1) contact resistance (10^{-6} to 10^{-5}, Peak 1), (2) intrinsic resistance (10^{-5} to 10^{-4}, Peak 2), (3) Li$^+$ penetration through the SEI layer/Li interface (10^{-4} to 10^{-3}, Peak 3), (4) impedance of Li$^+$ penetration through SEI/CPCEs (10^{-2} to 10^{-1}, Peak 4). Among them, the high impedance of P3 and 4 verifies the sluggish Li$^+$ transport across the interfacial double capacitor layer, which originates from the lithiophobicity and non-alloying Cu (Fig. 4c and e). Consequently, the resulting electrochemical hysteresis further exacerbates the decomposition of CPCEs and the accumulation of dead Li and an ionic-blocking layer. These effects collectively lead to disordered Li deposition and large polarization potential. In contrast, the interfacial ion transport resistance of the Li|Ag@CPCEs|Li symmetric cell gradually decreases from 220 Ω

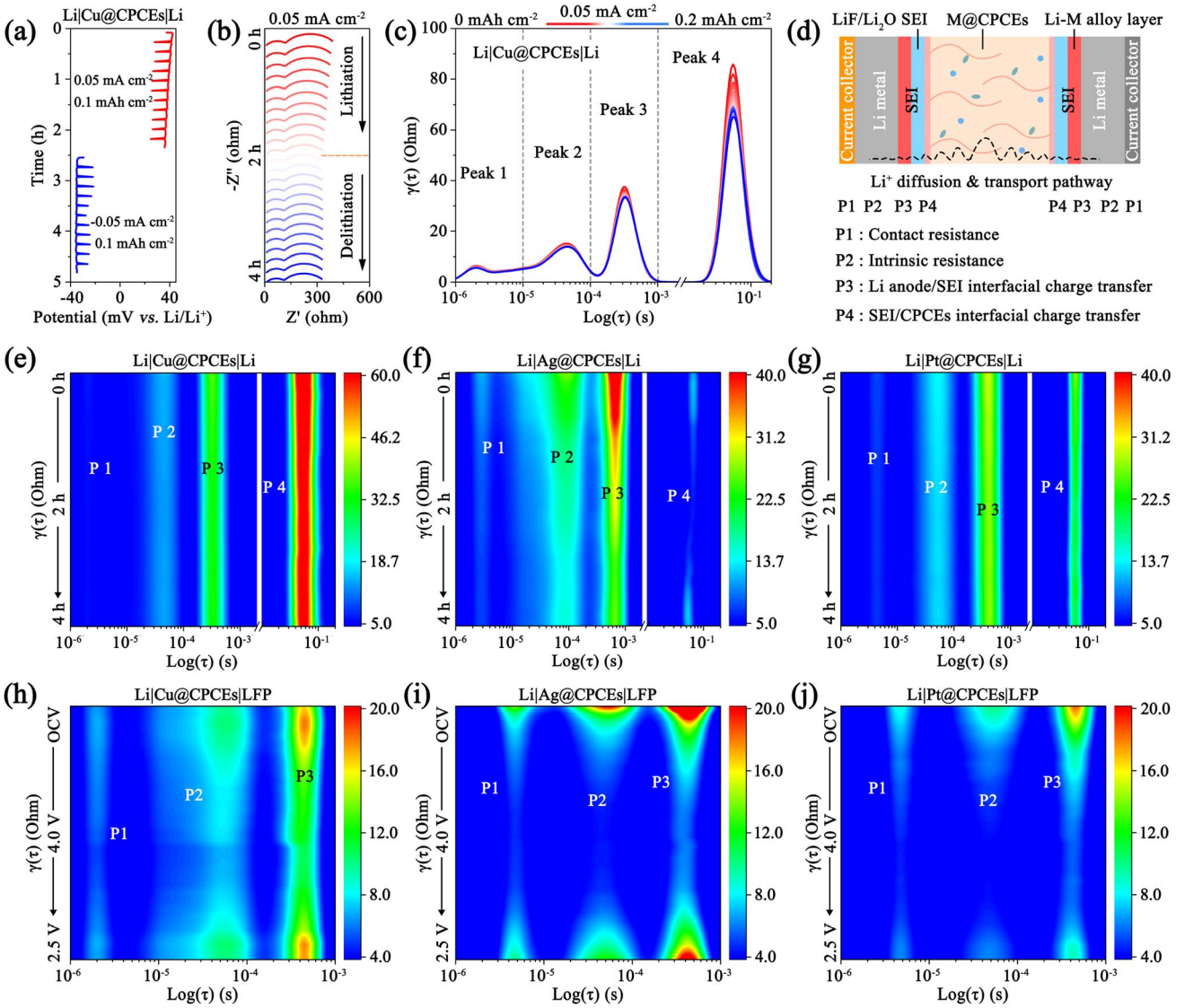

Fig. 4 EIS and DRT analyses of the Li||Li symmetric cell with the interfacial ion migration modulator. (a) Voltage profiles, (b) EIS and (c) DRT of the Li|Cu@CPCEs|Li symmetric cell under a cyclic current of 0.05 mA cm^{-2}, 0.1 mAh cm^{-2}, at 25 °C. (d) Schematic diagram of kinetic processes in the Li||Li symmetric cell with the interfacial ion migration modulator. DRT and contour map of (e) Cu@CPCEs, (f) Ag@CPCEs and (g) Pt@CPCEs-based Li||Li symmetric cells under 0.05 mA cm^{-2}, 0.1 mAh cm^{-2}, at 25 °C. DRT and contour map of (h) Cu@CPCE, (i) Ag@CPCE and (j) Pt@CPCE-based Li||LFP cells at 0.1C.

to 170 Ω, due to the favorable formation of a conductive Li–Ag alloy layer (Fig. S37b). However, the high impedance of P3 indicates that Li^+ transport through the Li/Li–Ag alloy/Li_2O–LiF SEI layer is impeded, due to the relatively lower diffusion rate of Li^0 within the Li–Ag alloy layer compared to the Li–Pt alloy (Fig. 4f, S37 and S38). What's more, the Pt based interfacial ion migration modulator can adjust the interfacial Li^+ transmission rate, thereby achieving a dynamic balance between the kinetics of Li^+ passage through the CPCEs/SEI interface and the Li/SEI interface (Fig. 4g and S38c, d).[37] The rapid interfacial ion transport and balanced interfacial electrochemistry promote the rapid interfacial Li^+ diffusion and uniform Li^0 nucleation, which contribute to achieving long-cycle stability.[38] To further evaluate the practical application, the Li||LFP cell with M@CPCEs was assembled and cycled at 0.1C with *in situ* EIS monitoring. The EIS analyses in Fig. 4i, j, S39 and S40 show that the interfacial resistances of the full cells based on Ag@CPCEs and Pt@CPCEs decrease rapidly with the Li^0 deposition, due to the formation of the artificial alloy layer. Conversely, the Cu@CPCE-based Li||LFP cell maintains a relatively high ion transport resistance, which prevents the theoretical capacity of LFP from being fully released (Fig. 4h and S41). Balancing the interfacial electrochemistry rate and constructing a stable and continuous ionic transport channel are the important methods to realize the rapid interfacial ion transport and obtain excellent interface stability.[39]

2.5 Performance of the interfacial ion migration modulator in QSSLMBs

To investigate the regulatory effect of the interfacial ion migration modulator on the ion transport kinetics in QSSLMBs, the Li|M@CPCEs|LFP cells were subjected to measurement of cyclic voltammetry (CV) and galvanostatic charge–discharge tests.[40] At the rate of 0.1 mV s^{-1}, the difference between the oxidation peak and reduction peak of the Pt@CPCE-based cell is only 332.0 mV, which is lower than those of Cu@CPCEs (536.0 mV), CPCEs (498.0 mV) and Ag@CPCEs (338.0 mV). This minimal voltage polarization can be attributed to the excellent interfacial ion transport regulation capability (Fig. S42). Subsequently, CV curves at different scan rates also verify that the hysteresis of Li conversion and transport at the Li|M@CPCEs|CPCE interface becomes more pronounced with the increase of current density, further exacerbating the kinetic hysteresis of ion transport. In contrast, Li|Pt@CPCEs|LFP has a low interfacial ion transport impedance, which enables a low peak voltage difference (789.0 mV) and the highest reduction peak current (−2.2 mA) even at 1.0 mV s^{-1} (Fig. S43). The kinetic characteristics of ion diffusion and transformation were further analyzed by plotting the peak current (I_p) against the square root of the scan rate. As shown in Fig. S44, the I_p values for the Li|Pt@CPCEs|LFP cell are 82.8 and −68.9, respectively, verifying the critical role of the Li–Pt alloy-based interfacial ion migration modulator in promoting the performance of the QSSLMBs.

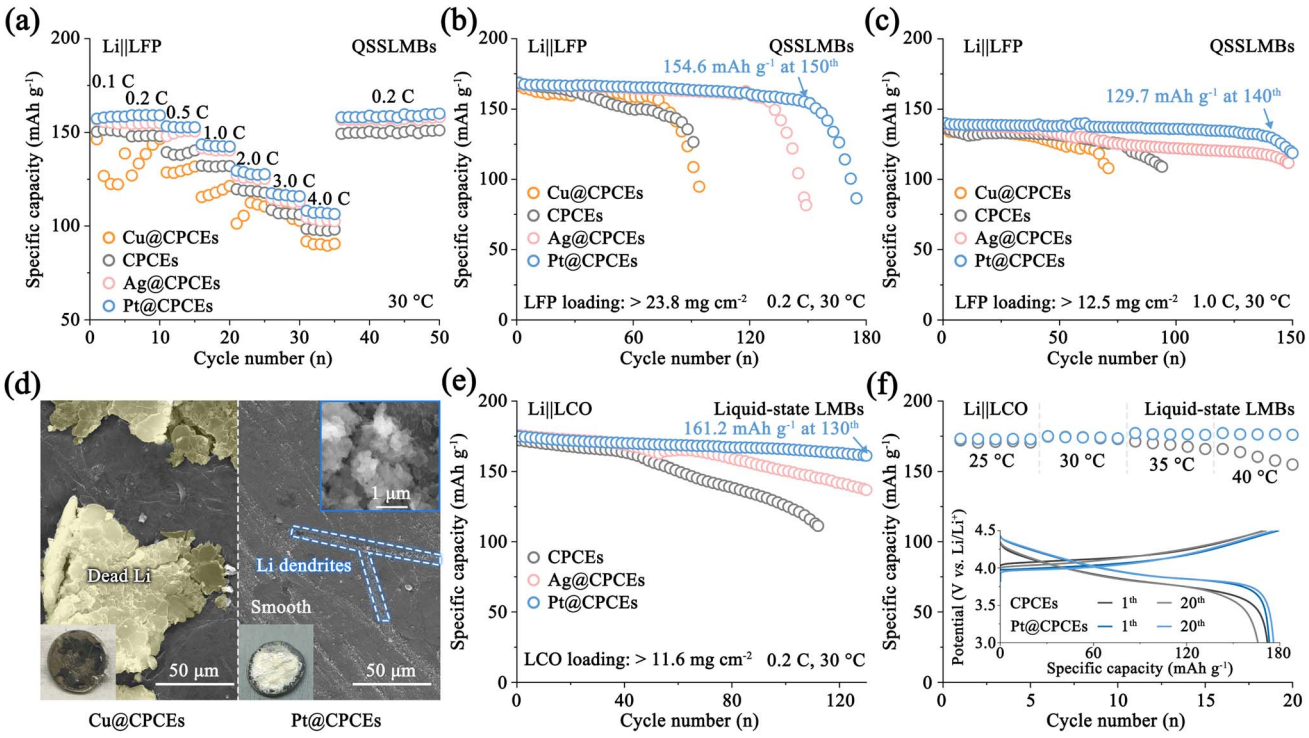

Fig. 5 Electrochemical performance of interfacial ion migration modulator-based LMBs. (a) Rate test section and (b and c) long-cycle tests of the Li||LFP QSSLMBs with the interfacial ion migration modulator at 30 °C. (d) SEM images and digital pictures of the Li metal interface within Li||LFP QSSLMBs after cycling. (e) Long-cycle tests of the Li||LCO liquid-state LMBs with the interfacial ion migration modulator under 0.2C, at 30 °C. (f) Long-cycle tests of the Li||LCO liquid-state LMBs with the interfacial ion migration modulator under 1.0C, at 25–45 °C.

The interfacial electrochemical rate balance enabled by the interfacial ion migration modulator was further assessed in Li||LFP cells through the rate capability test. The cell with Pt@CPCEs shows superior specific capacity, displaying discharge capacities of 157.4 (0.1C), 159.2 (0.2C), 153.3 (0.5C), 143.6 (1.0C), 129.6 (2.0C), 117.5 (3.0C), and 108.2 (4.0C) mAh g^{-1}, outperforming both the Cu@CPCE and bare CPCE-based cells (Fig. 5a). Moreover, when the current rate was restored to 0.2C, the discharge capacity recovers to158.1 mAh g^{-1}, which fully demonstrates the critical role of the interfacial ion regulation layer. To further verify that the modulator enhances the stability of the Li/CPCE interface, long-term cycling tests were conducted at 0.2C and 1.0C. As shown in Fig. 5b and S45, the Pt@CPCE-based cell maintains stable cycling performance at 0.2C, achieving a high specific capacity of 154.6 mAh g^{-1} at the 150th cycle. Conversely, the rapid capacity fade observed in Cu@CPCE and CPCE-based cells indicates the severe interfacial side reactions, which disrupt the electrochemical balance and accelerate CPCE decomposition and interface deterioration. Similarly, at a higher rate of 1.0C, the Li|Pt@CPCEs|LFP configuration also demonstrates excellent cycling stability with a capacity retention of 129.7 mAh g^{-1} after 140 cycles (Fig. 5c). The corresponding SEM images and digital pictures in Fig. 5d–f demonstrate the well-preserved surface morphology of Li metal regulated by the interfacial ion migration modulator after cycling for 50 cycles at 1.0C. Post-cycling analysis reveals a severely damaged Li anode with substantial dead Li in the Cu@CPCE-based cell.[41] To further validate the universality of this approach in regulating interfacial ion transport kinetics and balancing the interfacial electrochemical processes, Li|M@CPCEs|$LiCoO_2$ (LCO, 3.0–4.5 V) based liquid-state Li metal batteries were assembled. The Pt@CPCE-based cell shows 92.2% capacity retention (161.2 mAh g^{-1}) after 130 cycles at 0.2C (Fig. 5e and S46). By contrast, the CPCE-based Li||LCO cell experiences rapid capacity decay (73.0% at the 100th cycle) due to interface degradation. Consistent performance across 25–45 °C further highlights the modulator's robust electrochemical regulation (Fig. 5f). These findings fully demonstrate the universal effectiveness of artificial interface modification in regulating ion deposition and balancing interface electrochemistry (Fig. S47).

3 Conclusion

In summary, we propose an interfacial ion migration modulator to bridge the Li ion transport pathway between ceramic–polymer composite electrolytes and Li metal using a series of different lithiophilic nanoscale metals. Different metals such as Cu, Ni, Ag, Au and Pt were screened *via* theoretical simulation, spectroscopic measurement as well as electrochemical tests. The *in situ* formed Li–M alloy layer enhances Li^+ transport and nucleation kinetics, promoting uniform lateral deposition and (110)-oriented growth. Furthermore, the formation of the composite SEI structure (Li–M alloy/Li_2O–LiF) strengthens interfacial ion transport channels and suppresses the continuous CPCE deterioration and void formation, thereby achieving long-term cycling stability. Crucially, the composite Li–Pt/Li_2O–LiF SEI layer bridges the Li ion transport pathway and balances interfacial ion fluxes, preventing Li^+ heterogeneity and ensuring homogeneous deposition lasting for 1900 h. Consequently, the Pt@CPCE-based QSSLMB demonstrates exceptional cycling stability of 150 cycles at 0.2C, demonstrating a universal applicable strategy for stabilizing interfaces in SSLMBs.

4 Experimental section

Detailed experimental methods can be found in the SI.

Author contributions

Peng Chen conceived the idea, conducted the electrolyte preparation, battery-related experiments, and simulations, and prepared the draft manuscript. Hui Wang and Tianyu Wei conducted electrochemical measurements. Shengliang Zhang, Bing Ding, and Xiaogang Zhang participated in discussions. Hui Dou and Xiaogang Zhang contributed to manuscript editing, funding acquisition, and conceptualization.

Conflicts of interest

There are no conflicts to declare.

Data availability

All the data supporting this article have been included in the main text and the supplementary information (SI). Supplementary information is available. See DOI: https://doi.org/10.1039/d6sc00515b.

Acknowledgements

This work was supported by the National Natural Science Foundation Funded Project (52372199), National Key Research and Development Program of China (2023YFB2405800), Shenzhen Science and Technology Program (JCYJ20250604190043054), and Leading Edge Technology of Jiangsu Province (BK20232022, BK20220009). The authors are thankful for the support of the tests by the Center for Microscopy and Analysis, Nanjing University of Aeronautics and Astronautics.

References

1 X. Yang, M. Jiang, X. Gao, D. Bao, Q. Sun, N. Holmes, H. Duan, S. Mukherjee, K. Adair, C. Zhao, J. Liang, W. Li, J. Li, Y. Liu, H. Huang, L. Zhang, S. Lu, Q. Lu, R. Li, C. V. Singh and X. Sun, *Energy Environ. Sci.*, 2020, **13**, 1318–1325.
2 P. Chen, B. Ding, H. Dou and X. Zhang, *Small*, 2025, **21**, 2503743.
3 Q. Kang, Y. Li, Z. Zhuang, D. Wang, C. Zhi, P. Jiang and X. Huang, *J. Energy Chem.*, 2022, **69**, 194–204.

4 S. Lou, Q. Liu, F. Zhang, Q. Liu, Z. Yu, T. Mu, Y. Zhao, J. Borovilas, Y. Chen, M. Ge, X. Xiao, W. K. Lee, G. Yin, Y. Yang, X. Sun and J. Wang, *Nat. Commun.*, 2020, **11**, 5700.
5 P. Chen, P. Guo, W. Guo, B. Ding, H. Dou and X. Zhang, *J. Energy Chem.*, 2025, **110**, 363–371.
6 L. Lin, A. Ayyaswamy, Y. Zheng, A. Fan, B. S. Vishnugopi, P. P. Mukherjee and K. B. Hatzell, *ACS Energy Lett.*, 2024, **9**, 2387–2393.
7 X. Yang, X. Gao, S. Mukherjee, K. Doyle-Davis, J. Fu, W. Li, Q. Sun, F. Zhao, M. Jiang, Y. Hu, H. Huang, L. Zhang, S. Lu, R. Li, T. K. Sham, C. V. Singh and X. Sun, *Adv. Energy Mater.*, 2020, **10**, 2001191.
8 X. Yuan, B. Liu, M. Mecklenburg and Y. Li, *Nature*, 2023, **620**, 86–91.
9 Q. Xu, T. Li, Z. Ju, G. Chen, D. Ye, G. I. N. Waterhouse, Y. Lu, X. Lai, G. Zhou, L. Guo, K. Yan, X. Tao, H. Li and Y. Qiu, *Nature*, 2025, **637**, 339–346.
10 J. Xiao, *Science*, 2019, **366**, 426–427.
11 Q. Yang, C. Wang, L. Song, Y. Zhang, Z. Shen, W. Cai and Y. Song, *Angew Chem. Int. Ed. Engl.*, 2025, **64**, e202415078.
12 T. Wang, B. Chen, Y. Liu, Z. Song, Z. Wang, Y. Chen, Q. Yu, J. Wen, Y. Dai, Q. Kang, F. Pei, R. Xu, W. Luo and Y. Huang, *Science*, 2025, **388**, 311–316.
13 Z. Fan, B. Ding, B. Hu, Z. Li, D. Xiao, C. Xu, H. Dou and X. Zhang, *Electrochim. Acta*, 2022, **436**, 141441.
14 C. Zhao, Y. Tian, G. Sun, Y. Liu, X. Yang, R. Sun and X. Gao, *Adv. Funct. Mater.*, 2025, e12870.
15 Y. Peng, X. Xiong, W. Fan, W. Gao, X. Cheng, J. He, L. Fu, T. van Ree, T. Wang and Y. Wu, *Mater. Chem. Front.*, 2024, **8**, 1421–1450.
16 Y. Lu, C.-Z. Zhao, J.-Q. Huang and Q. Zhang, *Joule*, 2022, **6**, 1172–1198.
17 T. Xiao, J. Xian, Z. Yu, Z. Zhi, J. Zheng, W. Yan, K. Liu and P. Yang, *Angew Chem. Int. Ed. Engl.*, 2025, **64**, e202514027.
18 S. Chen, Q. Cao, B. Tang, X. Yu, Z. Zhou, S.-H. Bo and Y. Guo, *ACS Energy Lett.*, 2024, **9**, 5373–5382.
19 M. S. Kim, J. Wang, W. Zhang, P. Sayavong, Z. Zhang, S. T. Oyakhire, S. B. Shuchi, S. C. Kim, Y. Cui, Y. Chen, Z. Yu, H. Gong, R. Xu, J. Lee, I. R. Choi, J. H. Lee, K. A. Persson, J. Qin, Z. Bao and Y. Cui, *Nano Lett.*, 2025, **25**, 14625–14634.
20 J. Wang, J. Zhang, J. Wu, M. Huang, L. Jia, L. Li, Y. Zhang, H. Hu, F. Liu, Q. Guan, M. Liu, H. Adenusi, H. Lin and S. Passerini, *Adv. Mater.*, 2023, **35**, 2302828.
21 Q. He, Z. Deng, S. Miao, Y. Jia, J. Peng, P. Xia, C. Xu, Q. Tang, X. Zhang, T. Tan, G. Zhu, K. Wu, Y. Fang, Y. Zhang and W. Cai, *Energy Environ. Sci.*, 2025, **18**, 9093–9104.
22 F. Pei, L. Wu, Y. Zhang, Y. Liao, Q. Kang, Y. Han, H. Zhang, Y. Shen, H. Xu, Z. Li and Y. Huang, *Nat. Commun.*, 2024, **15**, 351.
23 F. Zhu, J. Wang, Y. Zhang, H. Tu, X. Xia, J. Zhang, H. He, H. Lin and M. Liu, *Adv. Mater.*, 2025, **37**, 2411601.
24 S. Liu, X. Liu, M. Chen, D. Wang, X. Ge, W. Zhang, X. Wang, C. Wang, T. Qin, H. Qin, L. Qiao, D. Zhang, X. Ou and W. Zheng, *Nano Res.*, 2022, **15**, 7199–7208.
25 Y. Liu, T. Yang, R. Fang, C. Lu, R. Ma, K. Yue, Z. Xiao, X. Zhou, W. Zhang, X. He, Y. Gan, J. Zhang, X. Xia, H. Huang, X. Tao and Y. Xia, *J. Energy Chem.*, 2024, **96**, 110–119.
26 D. He, W. Cui, X. Liao, X. Xie, M. Mao, X. Sang, P. Zhai, Y. Zhao, Y. Huang and W. Zhao, *Adv. Sci.*, 2022, **9**, 2105656.
27 Q. Li, Y. Liu, Z. Zhang, J. Chen, Z. Yang, Q. Deng, A. V. Mumyatov, P. A. Troshin, G. He and N. Hu, *Energy Environ. Mater.*, 2024, **7**, e12618.
28 N. F. Xavier and Q. Cai, *J. Power Sources*, 2025, **653**, 237567.
29 Z. Hui, S. Yu, S. Wang, G. Hyun, J. Holoubek, K. Zhou, J. Nicolas, M. Liu, Q. Miao, S. Tan, V. Petrova, H. Lin, J. Zhou, H. Liu and P. Liu, *Nat. Chem.*, 2026, **18**, 33–42.
30 K. Yan, Z. Lu, H.-W. Lee, F. Xiong, P.-C. Hsu, Y. Li, J. Zhao, S. Chu and Y. Cui, *Nat. Energy*, 2016, **1**, 16010.
31 C. Cui, H. Y. Yang, C. Zeng, S. Gui, J. Liang, P. Xiao, S. Wang, G. Huang, M. Hu, T. Zhai and H. Li, *Sci. Adv.*, 2022, **8**, eadd2000.
32 X. Yue, Y. X. Yao, J. Zhang, S. Y. Yang, W. Hao, Z. Li, C. Tang, Y. Chen, C. Yan and Q. Zhang, *Angew Chem. Int. Ed. Engl.*, 2025, **64**, e202413926.
33 Z. Sun, Y. Wang, S. Shen, X. Li, X. Hu, M. Hu, Y. Su, S. Ding and C. Xiao, *Angew Chem. Int. Ed. Engl.*, 2023, **62**, e202309622.
34 C. Xu, P. Jing, P. Xia, Y. Jia, J. Peng, Q. He, Q. Liu, Z. Song, X. Zhang, F. Wu, X. Liu, K. Wu, Y. Zhang and W. Cai, *Energy Environ. Sci.*, 2025, **18**, 7060–7070.
35 C. Xu, Z. Fan, J. Huang, L. Xu, B. Ding and X. Zhang, *Chem. Eng. J.*, 2025, **523**, 168549.
36 J. Pan, Z. Sun, X. Wu, T. Liu, Y. Xing, J. Chen, Z. Xue, D. Tang, X. Dong, H. Zhang, H. Liu, Q. Wei, D. L. Peng, K. Amine and Q. Zhang, *J. Am. Chem. Soc.*, 2025, **147**, 3047–3061.
37 Z. Song, Y. Ma, X. Cheng, Z. Zhu, Y. Zhong, J. He, T. Wang, D. Xu, Q. Zhang, K. I. Ozoemena, T. Brezesinski, Y. Ma, S. Passerini and Y. Wu, *Mater. Today*, 2025, **88**, 1005–1027.
38 J. Zhang, F. Liu, R. He, Q. Guan, N. Tian, J. Wu, Z. Cao, S. Yin, Y. Zhang, L. Jia, X. Li, C. You, H. Liu, M. Liu, Y. Miao, H. Lin and J. Wang, *Adv. Mater.*, 2025, e10894, DOI: 10.1002/adma.202510894.
39 K. Zhang, Q. Kang, J. Hua, Z. Wang, Y. Shi, H. Zhang, J. Wang, H. Zhu, R. Li, X. Zheng, G. Zhang, L. Huang, X. Fan and W. Luo, *Adv. Mater.*, 2025, e11616, DOI: 10.1002/adma.202511616.
40 Y. Yuan, D. D. Wang, Z. Zhang, K. T. Bang, R. Wang, H. Chen, Y. Wang and Y. Kim, *ACS Appl. Mater. Interfaces*, 2024, **16**, 44957–44966.
41 D. Weintz, L. Stolz, M. M. Bela, R. T. Hinz, M. Winter, M. Börner, I. Cekic-Laskovic and J. Kasnatscheew, *Adv. Energy Sustainability Res.*, 2025, **6**, 2500233.